ADVANCED MATERIALS
www.advmat.de

Ultrahigh-Loading Manganese-Based Electrodes for Aqueous Batteries via Polymorph Tuning

*Xin Xiao, Zewen Zhang, Yecun Wu, Jinwei Xu, Xin Gao, Rong Xu, Wenxiao Huang, Yusheng Ye, Solomon T. Oyakhire, Pu Zhang, Baoliang Chen, Emre Cevik, Sarah M Asiri, Ayhan Bozkurt, Khalil Amine, and Yi Cui**

Manganese-based aqueous batteries utilizing Mn^{2+}/MnO_2 redox reactions are promising choices for grid-scale energy storage due to their high theoretical specific capacity, high power capability, low-cost, and intrinsic safety with water-based electrolytes. However, the application of such systems is hindered by the insulating nature of deposited MnO_2, resulting in low normalized areal loading (0.005–0.05 mAh cm^{-2}) during the charge/discharge cycle. In this work, the electrochemical performance of various MnO_2 polymorphs in Mn^{2+}/MnO_2 redox reactions is investigated, and ε-MnO_2 with low conductivity is determined to be the primary electrochemically deposited phase in normal acidic aqueous electrolyte. It is found that increasing the temperature can change the deposited phase from ε-MnO_2 with low conductivity to γ-MnO_2 with two order of magnitude increase in conductivity. It is demonstrated that the highly conductive γ-MnO_2 can be effectively exploited for ultrahigh areal loading electrode, and a normalized areal loading of 33 mAh cm^{-2} is achieved. At a mild temperature of 50 °C, cells are cycled with an ultrahigh areal loading of 20 mAh cm^{-2} (1–2 orders of magnitude higher than previous studies) for over 200 cycles with only 13% capacity loss.

1. Introduction

The transition to a low-carbon economy and a sustainable future highlights the search for alternative clean energy technology. This has led to a surge in demand for advanced energy storage solutions, particularly in battery technologies with practical potential in grid-scale applications.[1] Despite the wide adoption of lithium-ion batteries in portable electronics and electric vehicles, the safety concerns of these organic-electrolyte-based batteries are driving the pursuit of alternative stationary storage solutions. Aqueous rechargeable batteries, based on non-flammable water-based electrolytes, hold great promise due to their environmental benignity, cost-effectiveness, high power capability, much-improved tolerance to mishandling, and reasonable energy density.[2–4] Additionally, the exemption of ultra-dry environment for manufacturing provides another competitive edge over the current LIB industry.[5]

Among various aqueous battery chemistries, manganese-based redox reactions have attracted wide attention.[6–10] The fact that manganese has multiple available valence states in aqueous solutions, including Mn(0), Mn(II), Mn(III), Mn(IV), and Mn(VII), has given rise to rich battery chemistries. Of all available redox couples, Mn^{2+}/MnO_2 presents attractive attributes such as high electrode potential (1.23 V vs standard hydrogen electrode (SHE)

X. Xiao, Z. Zhang, J. Xu, X. Gao, R. Xu, W. Huang, Y. Ye, P. Zhang, K. Amine, Y. Cui
Department of Materials Science and Engineering
Stanford University
Stanford, CA 94305, USA
E-mail: yicui@stanford.edu

Y. Wu
Department of Electrical Engineering
Stanford University
Stanford, CA 94305, USA

S. T. Oyakhire
Department of Chemical Engineering
Stanford University
Stanford, CA 94305, USA

B. Chen
Department of Environmental Science
Zhejiang University
Hangzhou, Zhejiang 310058, China

E. Cevik, S. M Asiri, A. Bozkurt, K. Amine
Bioenergy Research unit
Department of Biophysics
Institute for Research and Medical Consultations
Imam Abdulrahman Bin Faisal University
Dammam 31441, Saudi Arabia

K. Amine
Chemical Sciences and Engineering Division
Argonne National Laboratory
Lemont, IL 60439, USA

Y. Cui
Stanford Institute for Materials and Energy Sciences
SLAC National Accelerator Laboratory
2575 Sand Hill Road, Menlo Park, CA 94025, USA

The ORCID identification number(s) for the author(s) of this article can be found under https://doi.org/10.1002/adma.202211555

DOI: 10.1002/adma.202211555

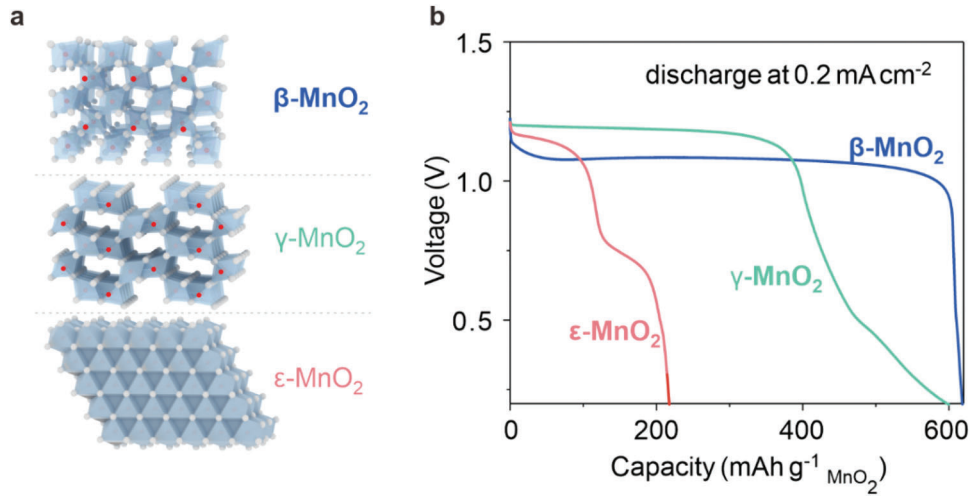

Figure 1. Electrochemical performance of ε-MnO_2, γ-MnO_2, and β-MnO_2-based cathode in aqueous electrolyte. a) Crystal structures of MnO_2 (red atoms: Mn; white atoms: oxygen). b) Cell voltage profile of ε-MnO_2, γ-MnO_2, and β-MnO_2 during discharge at a current density of 0.2 mA cm^{-2} in the Mn–H_2 battery (mass loading: ≈0.2 mAh cm^{-2}, electrolyte: 1 M $MnSO_4$ + 0.1 M H_2SO_4).

and high theoretical capacity (616 mAh g^{-1}). Recently, various types of aqueous batteries with Mn^{2+}/MnO_2 redox reactions have been reported for potential grid-scale energy storage, such as Mn–H_2,[11] Mn–Zn,[8,12–20] Mn–Cu,[21] Mn–Al,[22] Mn–Pb,[23] and Mn–Bi[24] batteries. Mn^{2+}/MnO_2 electrode follows the dissolution/precipitation reaction pathway as (Equation (1)).

$$Mn^{2+} + 2H_2O \leftrightarrow MnO_2\,(s) + 4H^+ + 2e^- \quad (1)$$

Upon charging, soluble Mn^{2+} gets oxidized into solid MnO_2 and deposited onto the current collector. The maximum specific areal loading is ultimately limited by the poor electronic conductivity of MnO_2. This can be more problematic for high-rate cycling. In fact, a highly reversible Mn^{2+}/MnO_2 electrode often requires a porous, high-surface-area, and electronically conducting substrate, where only a thin layer of MnO_2 is deposited to shorten the electron transport distance to guarantee the reversible electrode reactions. It is still challenging to achieve high loading in a Mn^{2+}/MnO_2 electrode to realize the practical application.

Polymorphism, the ability of solid materials to crystallize into various crystal structures with the same stoichiometry, adds another dimension to functionality tuning over materials. MnO_2 is a widely investigated polymorphic inorganic material in catalysis,[25,26] water desalination,[27] and energy storage,[28–32] featured by various arrangements of edge or corner-sharing [MnO_6] octahedra units.[33] Such variations in different morph structures give rise to dramatically different chemical, physical, and biological properties, having direct impact on their function properties and thus on their technological applications.[34]

Herein, we investigated the electrochemical performance of various MnO_2 polymorphs in Mn^{2+}/MnO_2 redox reactions and determined that the primary electrochemically deposited MnO_2 phase in the acidic aqueous electrolyte is ε-MnO_2 with low conductivity. We discovered that we could tune the deposited phase of MnO_2 with temperature and exploit the highly conductive polymorphs to achieve a highly reversible and ultrahigh areal loading MnO_2 cathode for aqueous batteries. As temperature rises, the deposited phase gradually changes from ε-MnO_2 to γ-MnO_2, with over two orders of magnitude increase in conductivity. At a mild temperature of 50 °C, cells were cycled with an ultrahigh areal loading of 20 mAh cm^{-2} for over 200 cycles with only 13% capacity loss.

Table 1. The electrical conductivity of various MnO_2 polymorphs.

MnO_2 phase	α	β	γ	δ	ε	λ
Conductivity [mS m^{-1}]	111.2	974.8	403.1	3.7	2.0	3.7

2. Results and Discussion

2.1. Electrochemical Performance of MnO_2 Polymorphs

Typical polymorphs of MnO_2 for energy storage and other applications include α-, β-, γ-, δ-, ε-, and λ-MnO_2. These polymorphs differ in the way of interlinkage between the MnO_6 octahedra, resulting in tunnels or interlayers with various magnitudes of gaps (**Figure 1**a; Figure S1, Supporting Information). We synthesized all six MnO_2 polymorphs[25,35–39] and confirmed their crystalline structures with X-ray powder diffraction (XRD) (Figure S2, Supporting Information). The measured electronic conductivities of MnO_2 polymorphs via the four-point probe method are summarized in **Table 1**. Among the polymorphs, δ-, λ-, ε-MnO_2 have similar electronic conductivities ≈2 mS m^{-1}, while α-, β-, and γ-MnO_2 show much better electrical conductivities about two orders of magnitudes higher, agreeing well with previous experimental reports (Table S1, Supporting Information)[40–43] and theoretical bandgap computation.[44] These MnO_2 polymorphs were further made into slurry-coated electrodes and cycled in an aqueous electrolyte. A threefold difference in specific discharge capacity was observed among all the polymorphs. Specifically, β-MnO_2, the morph with the highest electrical conductivity, delivers the highest specific capacity of 616.0 mAh g^{-1}_{MnO2}, while ε-MnO_2

delivers only 217.3 mAh g^{-1}_{MnO2}. (Figure 1b) Polymorphs with comparable electrical conductivity as β-MnO_2, for example, γ-MnO_2, deliver a specific capacity of 597.4 mAh g^{-1}_{MnO2} (Figure 1b), quite close to MnO_2's theoretical capacity of 616 mAh g^{-1}_{MnO2}, showing excellent electrochemical performance. In general, the electrochemical performance of MnO_2 polymorphs in Mn^{2+}/MnO_2 redox reactions follows a similar trend in their electrical conductivities, which work not only in Mn–H_2 batteries (Figure S1d, Supporting Information) but also in Mn–Zn batteries (Figure S3, Supporting Information). Figure 1b shows the typical discharge curves of ε-MnO_2, γ-MnO_2, and β-MnO_2 electrodes.

2.2. Primary Phase of Electrochemically Deposited MnO_2 in Aqueous Electrolyte

Despite the significant difference in electrochemical performance of various MnO_2 polymorphs, the primary phase, or phases, of electrochemically deposited MnO_2 in aqueous electrolytes remain largely uninvestigated for secondary mildly acidic aqueous Mn^{2+}/MnO_2 batteries. Here, we found that the primary phase of electrochemically deposited MnO_2 in common aqueous electrolytes is ε-MnO_2 (**Figure 2**a–f). The lowest electronic conductivity among all polymorphs makes ε-MnO_2 the least favorable for electrochemical reactions. The high performance of ε-MnO_2 in previous reports arose from a low specific normalized areal loading (0.005–0.05 mAh cm^{-2}) on current collector.[11,45] However, high energy density and low-cost battery entail practically high areal loading of active materials with improved reversibility. Specifically, cycling with MnO_2 polymorphs of higher electrochemical reversibility is the key. This becomes increasingly critical for the Mn^{2+}/MnO_2 electrode as new solid MnO_2 forms in every cycle, which directly impacts the overall electrochemical performance of the battery. The electrode with as-synthesized β-MnO_2 completely dissolved during the first discharge cycle. Both the scanning electron microscopy (SEM) and XRD (Figure 2a,b) confirmed the existence of β-MnO_2 at the initial state, and no XRD peak of β-MnO_2 was detected after discharge. After the second charge cycle at 0.2 mA cm^{-2} for 40 min, the newly deposited phase became ε-MnO_2 (Figure 2a,b).

Polymorphism can be affected by the details of crystallization.[46] The solvent in all aspects affects the nature of the polymorph, including concentration, inhibiting, or promoting certain growth patterns. We deposited MnO_2 to 1 mAh cm^{-2} in electrolytes with various Mn^{2+} concentrations, from 0.1 to 3 M, and found that the ε-MnO_2 with low conductivity was the primary deposited phase (Figure 2c). Despite the increase in current density from 0.01 to 5 mA cm^{-2}, the primary polymorph deposited remained to be ε-MnO_2 with the characteristic 2θ peaks (Mo source) at 16.8°, 19.2°, 25.0°, and 29.4° (JCPDS card 00-030-0820) (Figure 2d). Furthermore, we checked the effect of substrate. On Au, Ag, Pt, Ru, stainless steel (SS), and graphite, substrates that are compatible with Mn^{2+}/MnO_2 redox reactions, the deposited phases were all ε-MnO_2 (Figure 2e). Note that the above experiments were carried out on bare current collectors without preloaded MnO_2. In addition, we discovered that the growth of MnO_2 cannot be altered by growing on a certain morph (Figure S4, Supporting Information). When the electrode with preloaded β-MnO_2 was charged, the increasing peak intensity at 29.4° (ε-MnO_2) and the decrescent peak at 13.4° (β-MnO_2) indicated that the primary deposited MnO_2 phase was still ε-MnO_2. Although the above analysis was done in a Mn–H_2 battery, the same observation is true in Mn–Zn batteries (Figure S4, Supporting Information).

2.3. Polymorph Tuning of the Electrochemically Deposited MnO_2 via Temperature

Since the lattice energy differences between polymorphs are usually small,[47] we hypothesize that it is possible to tune the polymorphs by slightly adjusting the temperature of the solvent in which the crystallization is carried out. Layer-to-tunnel (L-T) transition was observed in Mg^{2+}-buserite after hydrothermal treatment at 220 °C,[48–50] confirming the temperature-dependent polymorph manipulation. Here, we cycled the battery at different temperatures to alter the deposited MnO_2 polymorphs (**Figure 3**). The batteries were rested for 30 min before cycling to ensure temperature equilibrium. We found that as the temperature increased from 25 °C to 90 °C, there was a transition in deposited phase from ε-MnO_2 to γ-MnO_2 (Figure 3a). At 50 °C, there was a mixture of ε-MnO_2 and γ-MnO_2, while at 90 °C γ-MnO_2 was the only morph deposited. Though in the industry and research field, preparation of electrolytic manganese dioxide (mainly γ-MnO_2) at high temperature has been reported for the application in alkaline batteries, lithium manganese primary batteries, and supercapacitors,[51–53] this temperature-dependent polymorphism tuning is seldom reported for cycling Mn-based aqueous batteries under a two-electron transfer mechanism. In the corresponding XRD spectra (Figure 3b), the increasing peak intensities at $2\theta = 10.0°$ (Mo sources) and the decreasing peak intensities at $2\theta = 29.4°$ (Mo sources) were in accord with such a crystallographic transition. The morphological changes of the deposited MnO_2 at different temperatures shown in Figure 3d–g transitioned from a round-shaped particle at room temperature (25 °C) to a more needle-shaped overall structure at higher temperatures. Such morphology and phase transition under various temperatures were also confirmed in Mn–Zn batteries (Figure S5, Supporting Information).

The electronic conductivity of γ-MnO_2 is two orders of magnitude higher than ε-MnO_2 (Table 1). Such a less resistive deposited phase enables higher areal capacity loading in principle. We measured the ohmic resistance of the deposited MnO_2 layer as a function of the deposited capacity, where the ohmic resistance from electrolyte/current collectors and proton concentration was corrected beforehand. The slope reflects the electronic resistivity of the deposited phase, where a smaller slope indicates a smaller resistivity. As shown in Figure 3c, the slope gets smaller as the temperature increases. Such a change corresponds well with the observed transition from the more resistive morph ε-MnO_2 to a more conductive morph γ-MnO_2.

2.4. Ultrahigh-Loading Manganese-Based Electrode via Polymorph Manipulation

To demonstrate the advantage of polymorph tuning in Mn^{2+}/MnO_2 reactions, we compared the total areal capacity

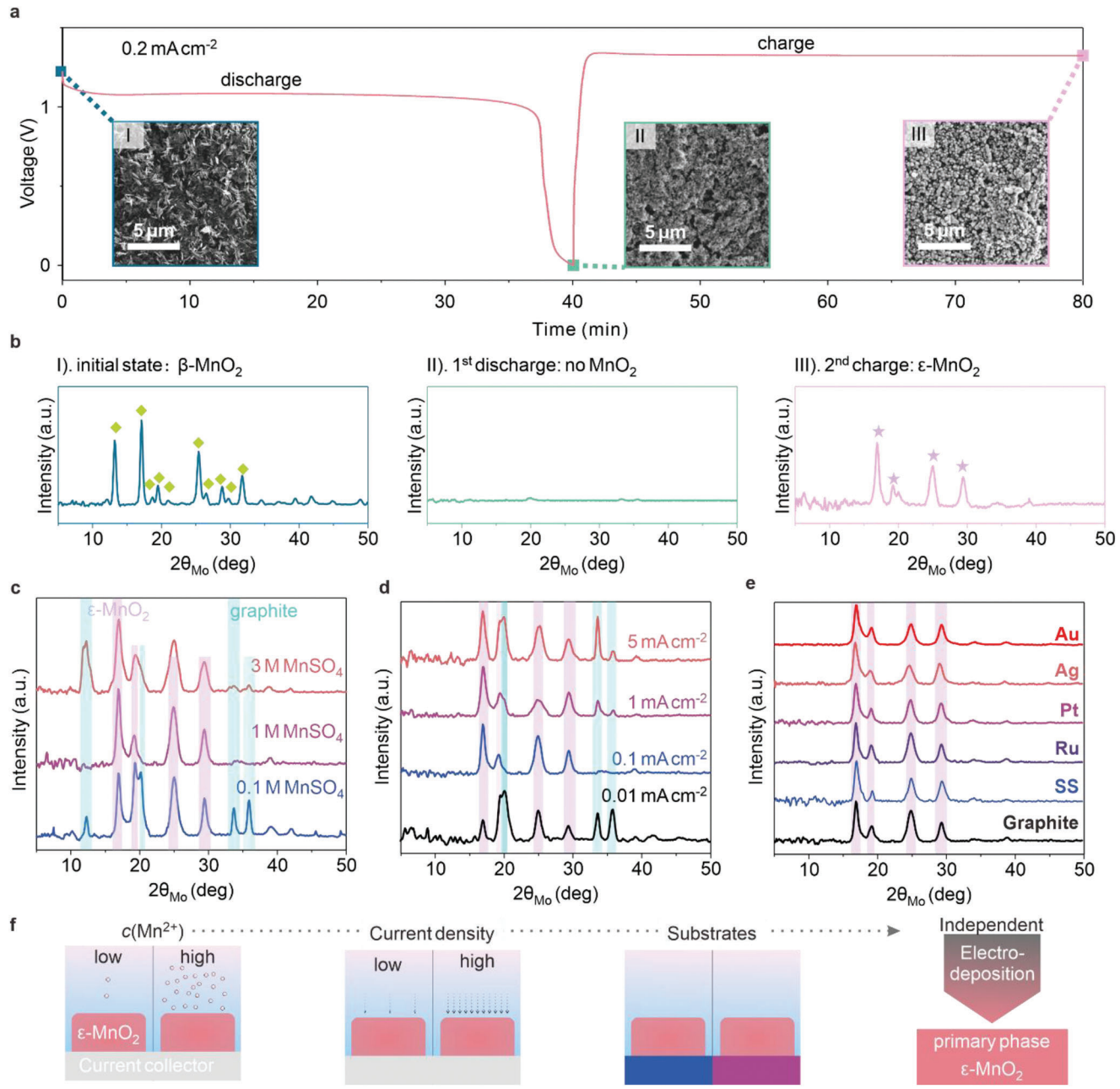

Figure 2. The primary phase of electrochemically deposited MnO_2 in aqueous electrolyte. a) The discharge curve of β-MnO_2-based cathode and the following charge curve. The inset SEM images show the cathode morphology at the initial state, after 1st fully discharge, and after 1st charge, respectively. b) Corresponding XRD spectra of the cathode at different states in Figure 2a. The green diamonds and the pink stars indicate the diffraction peaks of β-MnO_2 (JCPDS card 00-024-0735) and ε-MnO_2 (JCPDS card 00-030-0820), respectively. c) XRD spectra of MnO_2 deposited in electrolytes with different Mn^{2+} concentrations. d) XRD spectra of MnO_2 deposited at various current density in 1 M $MnSO_4$ + 0.1 M H_2SO_4 electrolyte. e) XRD spectra of MnO_2 deposited on different substrates in 1 M $MnSO_4$ + 0.1 M H_2SO_4 electrolyte. The pink bars indicate the diffraction peaks of ε-MnO_2 and the cyan bars indicates the diffraction peaks of graphite current collector (JCPDS card 04-014-0362). "SS" denotes stainless steel. f) Summarized schematic diagram of the primary deposited phase under various conditions. Note that current collector used in Figure 2 is graphite foil unless specified.

achievable with a constant current (10 mA cm^{-2}) and a voltage cutoff (1.6 V) at different temperatures. Notice that a flat graphite foil was used as the current collector as a model system (Figure S6, Supporting Information) to avoid the normalization of high surface areas in other 3-D current collectors. **Figure 4**a shows the typical charge/discharge curves of batteries at 25 and 75 °C at 10th cycle. The total charge capacity of ≈35 mAh cm^{-2} and a discharge capacity of 33 mAh cm^{-2} were achieved at 75 °C. In contrast, a charge capacity of 0.02 mAh cm^{-2} with a discharge capacity of 0.01 mAh cm^{-2} was achieved at 25 °C. A 2000-fold increase in the areal mass loading of MnO_2 was observed. Such drastic improvement demonstrated the power of polymorph

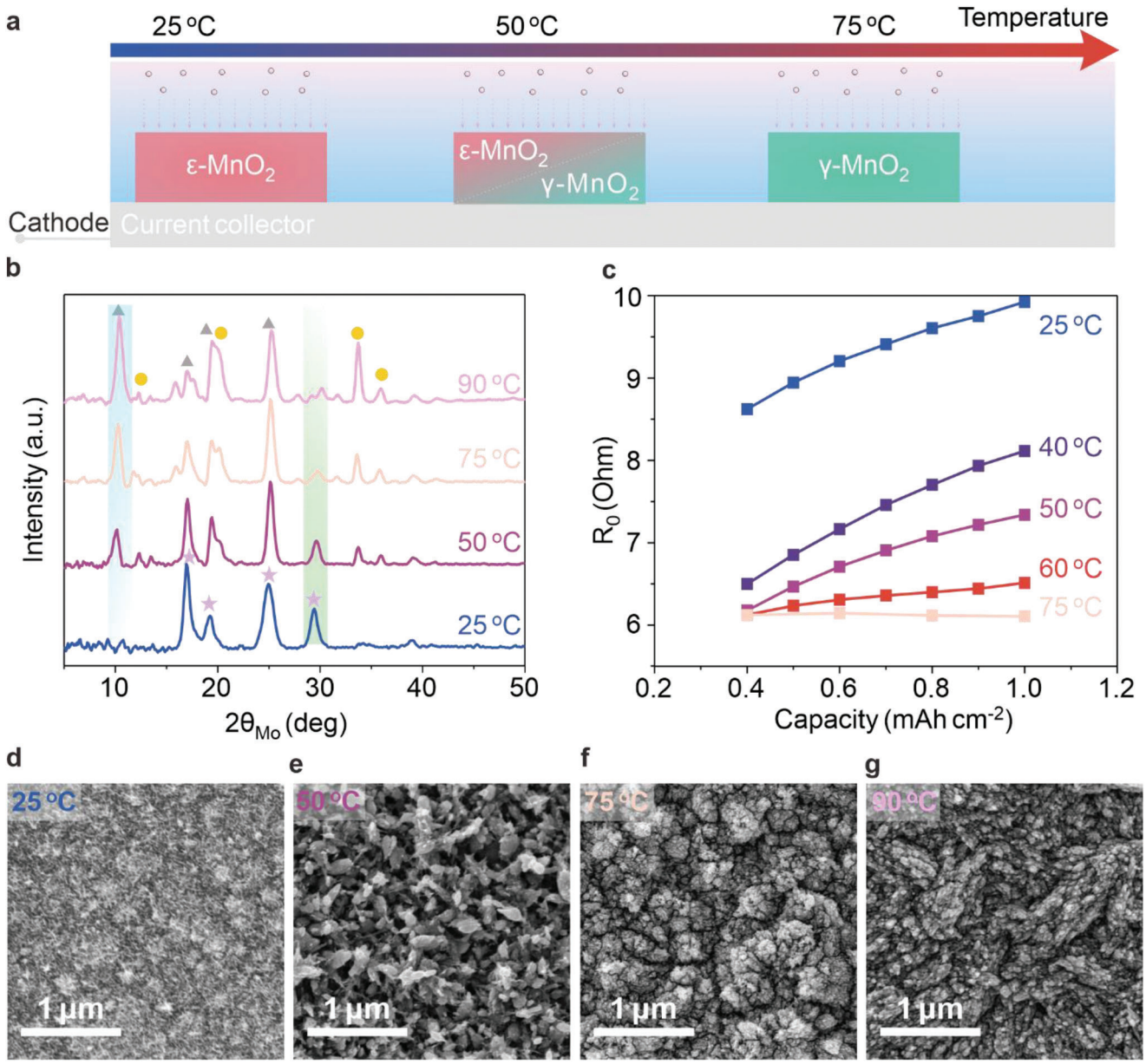

Figure 3. Temperature dependence of electrochemically deposited MnO_2 phase. a) Schematic of deposited MnO_2 polymorph transition as a function of temperature. b) XRD patterns of deposited MnO_2 at different temperatures. The pink stars, gray triangles, and yellow circles refer to ε-MnO_2, γ-MnO_2, and graphite, respectively. c) Cell resistance as a function of the deposited capacity of MnO_2 at different temperatures. Current collector: graphite foil. The battery was first charged at 1.6 V to certain capacity and rested for 5 min before the electrochemical impedance spectroscopy (EIS) measurement. Note that the resistance R_0 was after proton concentration correction, such that the slopes of these curves reflect the electronic resistance increment per 1 mAh cm^{-2} MnO_2 deposited. d–g) The SEM images of deposited MnO_2 on a graphite foil current collector at different temperatures (0.1 mA cm^{-2} to 1 mAh cm^{-2}).

tuning in building ultra-high loading Mn-based electrodes. Figure 4b shows the cross-sectional SEM images and corresponding energy-dispersive spectrometry (EDS) mapping of the deposited MnO_2 layers at 25 and 75 °C after 1st cycle charge. More thickness variation of MnO_2 layer by cycles could be found in Figure S7 (Supporting Information). The thickness (≈45 μm) of the deposited MnO_2 at 75 °C is remarkably larger than the thickness (<1 μm) of MnO_2 at 25 °C. To show that the increase in discharge capacity was the result of a more favorable morph instead of other factors influenced by temperature, such as the ionic conductivity in the electrolyte, we charged the battery at 75 °C to deposit more conductive γ-MnO_2, and then cooled down the battery to room temperature for discharge. A comparable Coulombic efficiency (CE) was obtained compared with CE of cycled cells at 75 °C (75.7% vs 81.5%). In contrast, batteries both charged and discharged at 25 °C showed a CE of only 15.7% (Figure 4c). These results indicated that the increased conductivity of a more favorable morph contributed substantially

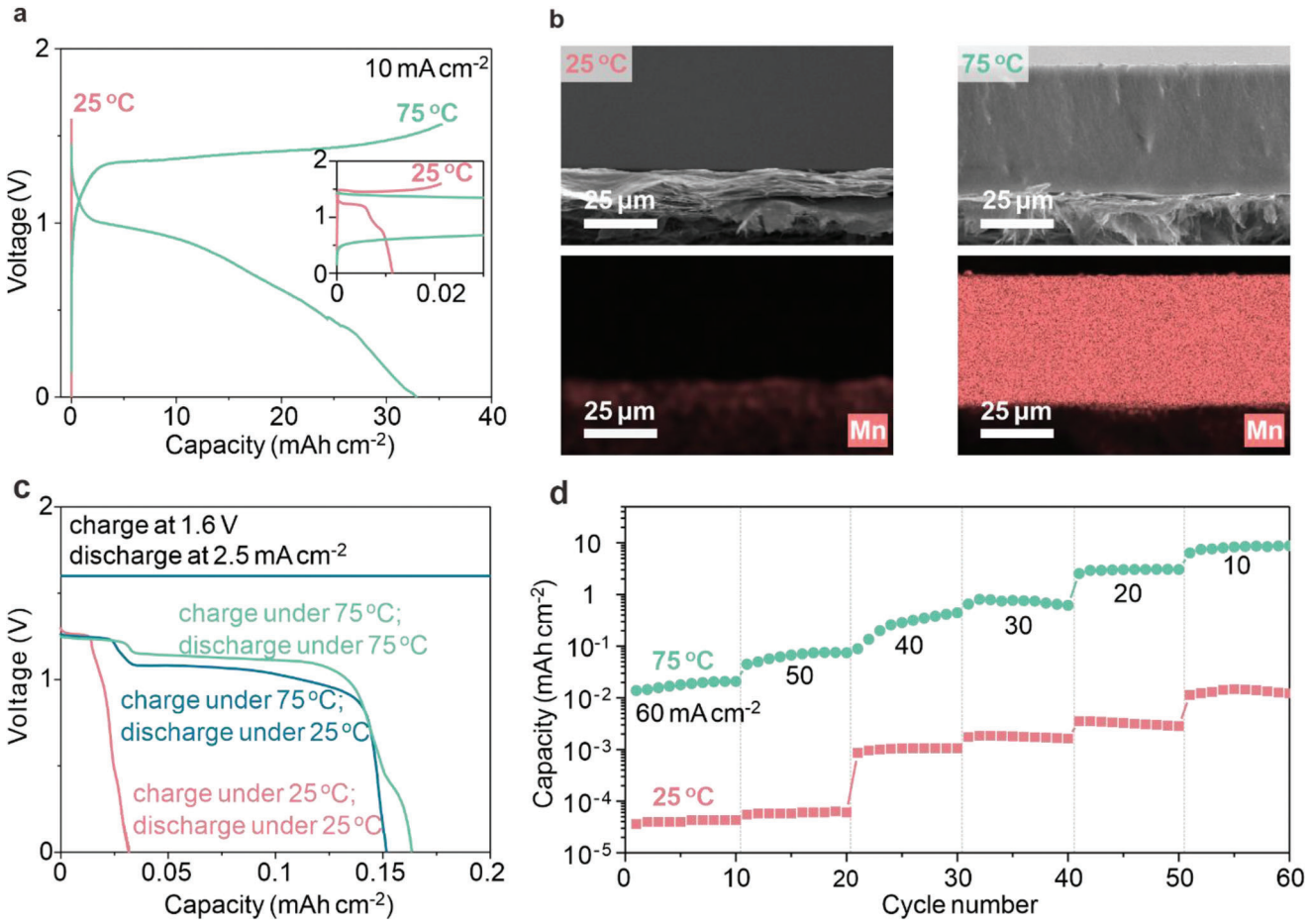

Figure 4. Ultrahigh areal loading MnO_2 electrode enabled by polymorph manipulation. a) Charge–discharge curve in a Mn–H_2 battery using cathode graphite foil under different temperature using large volume of electrolyte (100 mL 1 M $MnSO_4$ + 0.1 M H_2SO_4). The inset is the zoom-in diagram of areal capacity up to 0.03 mAh cm^{-2}. b) Cross-sectional SEM images and the corresponding EDS mapping of the deposited MnO_2 layer on graphite foil after 1st charge cycle at 10 mA cm^{-2}; scale bar: 25 µm. c) Discharge curve under different charge/discharge temperatures. d) Rate capability of the MnO_2 deposited at 25 and 75 °C.

to the CE increase. Moreover, these findings also highlight the need to maintain a comparatively high operating temperature while depositing MnO_2 to ensure a high capacity. We also show that such 2–3 orders of magnitude increase in the areal loading of MnO_2 was maintained over a wide current density range (Figure 4d).

2.5. Mn–H_2 Cell Performance with High Areal MnO_2 Loading

To evaluate the cell performance of Mn^{2+}/MnO_2 electrodes with polymorph tuning in a more applicable setting, we tested the batteries at 50 °C in a Mn–H_2 battery setup as shown in **Figure 5**a. Two different charging protocols were applied here. Figure 5b shows the result of charging with constant current to compare the area mass loading under 100 mA cm^{-2}. For room temperature without phase regulation, the discharged MnO_2 was 0.51 mAh cm^{-2}, with a comparison to the discharged capacity of 23.4 mAh cm^{-2} after phase regulation (50 °C), implying a two orders of magnitude increment in MnO_2 areal loading. Figure 5c shows the result of charging with constant voltage to a fixed capacity to compare the Coulombic efficiency. Both cells were charged under 1.6 V to 20 mAh cm^{-2}, the discharged capacity at 200 mA cm^{-2} was only 0.15 mAh cm^{-2} under 25 °C, substantially lower than 17.7 mAh cm^{-2} under 50 °C. The corresponding SEM images of the carbon felt current collector after discharge showed that a nontrivial amount of MnO_2 deposit remained under 25 °C, while little could be observed under 50 °C (Figure 5e,f). The improved performance could also be observed under other current densities (Figure S8, Supporting Information).

We further tested the long-term cycle performance with two high areal capacities, 10 and 20 mAh cm^{-2}. Figure S9 (Supporting Information) shows the cycling data for 10 mAh cm^{-2} loading under 25 and 50 °C. An extended cycle life of 450 cycles under 50 °C was achieved, compared to 296 cycles at 25 °C. More importantly, a much faster overpotential increase was observed at 25 °C due to the irreversible loss of available conductive surface from incomplete MnO_2 dissolution. Post-mortem investigation on the 100-cycled cathode indicated a less remaining MnO_2 particles on carbon fiber for battery cycling at higher temperatures; and neither carbon expansion nor carbon exfoliation was detected, suggesting the stability of the carbon current collector

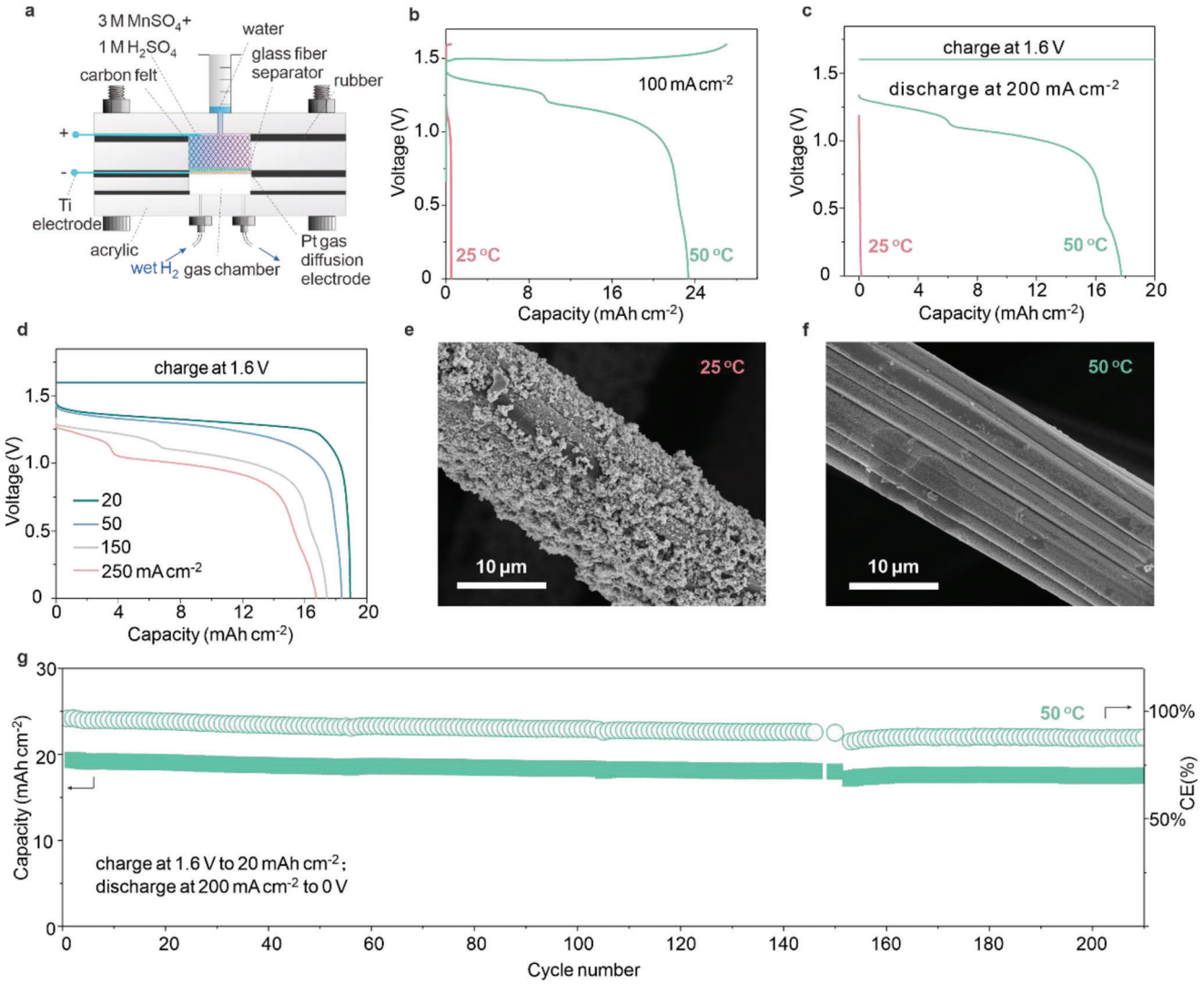

Figure 5. Cycling performance based on temperature dependent MnO_2 regulation using carbon felt as cathode. a) Schematic diagram of Mn–H_2 cell using carbon felt as cathode current collector. b) The 1st cycle difference by temperature under galvanostatic charge/discharge profile (100 mA cm^{-2}). c) The temperature effect of Mn–H_2 battery under potentiostatic charge at 1.6 V to 20 mAh cm^{-2}, then discharge at 200 mA cm^{-2} to 0 V. d) The discharge curve of Mn–H_2 battery at 50 °C under different current densities. e,f) The morphologies of the carbon felt after 1st cycle discharge from (c) at 25 and 50 °C, respectively. g) The long cycle performance of Mn–H_2 under a mass loading of 20 mAh cm^{-2} (charged at 1.6 V), and discharged at 200 mA cm^{-2}, followed by a deep discharge current of 20 mA cm^{-2} in every cycle.

during cycling (Figure S9e,f, Supporting Information). With a more concentrated Mn^{2+} electrolyte (3 mol L^{-1}), a higher areal capacity loading of 20 mAh cm^{-2} could be achieved, with a cycle life of over 200 cycles and only 13% capacity loss. It should be noted that no comparable high areal loading was reported previously in Mn^{2+}/MnO_2-based aqueous batteries with conventional separators.

3. Conclusion

This work investigated the electrochemical performances of MnO_2 polymorphs for Mn^{2+}/MnO_2 electrodes in acidic aqueous electrolytes. The primary electrochemically deposited phase in the conventional aqueous electrolyte is ε-MnO_2, which has the lowest electronic conductivity and thus poor electrochemical performance. We demonstrated temperature as an effective tuning knob in polymorph tuning to manipulate the deposited phase of MnO_2. With a mild increase in temperature, the electrochemically deposited MnO_2 phase transitions from ε-MnO_2 to γ-MnO_2, whose electronic conductivity is high enough to enable ultrahigh areal loading of the MnO_2 cathode with superior rate capability and reversibility. As a proof of concept, the battery can be cycled at 20 mAh cm^{-2} for over 200 cycles with only 13% capacity decay. Such ultrahigh areal loading cathode substantially lowers the overall cost and promises the practical application of manganese-based batteries for grid-scale energy storage. We expect this polymorphism tuning to be generally applicable to dissolution/precipitation battery chemistry, engineering high energy density aqueous batteries, and beyond.

4. Experimental Section

Materials Synthesis: MnO_2 polymorphs were synthesized via hydrothermal methods. XRD spectra of corresponding MnO_2 polymorphs (Figure S2, Supporting Information) matched well with the standard JCPDS cards, confirming the crystal structures of the obtained MnO_2. The corresponding detailed synthesis procedures were listed as follows:

α-MnO_2 (JCPDS: 00-044-0141): $KMnO_4$ (1.26 g) and $MnSO_4{\cdot}H_2O$ (0.51 g) were dissolved in 80 mL deionized water (DI water) and stirred for 30 min. The mixture solution was transferred into a Teflon-lined stainless-steel reactor. The autoclave was then heated at 160 °C with a ramp up rate of 10 °C min^{-1} and held for 12 h. After cooling down to room temperature, the solid precipitates were washed with DI water eight times and collected with centrifuging to remove the residual salts. The powders were dried overnight at 80 °C and then calcined at 300 °C for 4 h to yield a brown powder.

β-MnO_2 (JCPDS: 00-024-0735): $NaMnO_4{\cdot}H_2O$ (1.28 g) and $MnSO_4{\cdot}H_2O$ (2.03 g) were dissolved in 40 mL DI water and stirred for 30 min. The mixture solution was transferred to a Teflon-lined stainless-steel reactor. The autoclave was then heated at 160 °C with a ramp up rate of 10 °C min^{-1} and held for 12 h. After cooling down to room temperature, the solid precipitates were collected after centrifuging and washing with DI water eight times to remove the residual salts. The powder was dried overnight at 80 °C.

γ-MnO_2 (JCPDS: 00-014-0644): $MnSO_4{\cdot}H_2O$ (1.35 g) was first dissolved in 30 mL DI water, and 1.83 g of $(NH_4)_2S_2O_8$ was added to the solution. After stirring for 30 min, the mixture solution was then water-bathed with stirring (800 rpm) at 90 °C. After cooling down to room temperature, the solid precipitates were collected after centrifuging and washing with DI water for eight times to remove the residual salts. The powder was dried overnight at 80 °C.

δ-MnO_2 (JCPDS: 01-073-7867): $KMnO_4$ (3 g) was first dissolved in 50 mL DI water, and 20 mL 1.4 mol L^{-1} glucose aqueous solution was added. After a 2 h reaction at room temperature, a brown gel was obtained. The gel was dried at 110 °C for 24 h and then calcined at 400 °C for 2 h. After cooling down to room temperature, the solid precipitates were collected after centrifuging and washing with DI water eight times to remove the residual salts. The powder was dried overnight at 80 °C.

ε-MnO_2 (JCPDS: 00-030-0820): $Fe(NO_3)_3{\cdot}9H_2O$ (2.15 g) was first dissolved in 100 mL DI water, and 3.45 g of $MnCO_3$ was added. The solution was stirred for 30 min. Next, 2 mL concentrated H_2SO_4 was added, followed by the addition of 6.85 g of $(NH_4)_2S_2O_8$. Finally, 50 mL DI water was added. After stirring for 30 min, the solution was transferred to a Teflon-lined stainless-steel reactor. The autoclave was then heated to 110 °C with a ramp-up rate of 10 °C min^{-1} and held for 3 h. After cooling down to room temperature, the solid precipitates were collected after centrifuging and washing with DI water eight times to remove the residual salts. The powder was dried overnight at 80 °C.

λ-MnO_2 (JCPDS: 00-044-0992): $LiMn_2O_4$ was first synthesized as the precursor of λ-MnO_2. Briefly, 1.224 g of $Mn(CH_3COO)_2{\cdot}4H_2O$ and 0.17 g of $LiNO_3$ were dissolved in 10 mL DI water. The 10 mL aqueous solution contained 2.88 g of citric acid and 0.90 g of urea was added. Nitric acid (2 mL) was then added. The solution was kept under stirring for 5 min. The solution was then heated and kept at 80 °C to remove all the solvent for 3 days. The remaining precipitate was dried at 170 °C for 12 h and calcined at 350 °C for 12 h to become a gray powder. The as-obtained $LiMn_2O_4$ was mixed with 22 mL DI water, followed by adding 28 mL 0.1 mol L^{-1} HNO_3.The mixture was then stirred and sonicated for 2 h. The solid precipitates were filtrated and washed with DI water eight times to remove the residual salts. The powder was dried overnight at 80 °C.

Electrical Conductivity Measurement: The four-point probe method was used to measure the electronic conductivities of MnO_2 polymorphs.[41,54] The schematic of the four-point probe method is shown in Figure S1b (Supporting Information). Specifically, 0.2 g MnO_2 powder was weighted and pressed under 2 ton cm^{-2} for 5 min into a pellet with a 1 cm^2 circle and 1 mm thickness. The thickness of each pellet was measured by a slide caliper. Next, four copper wires were connected to the pellet with the silver paste. The voltage responses of two points (i.e., $V_{1,2}$) were recorded while applying different current to the other two points (i.e., $I_{3,4}$) using the Keysight B1500A Semiconductor Device Analyzer. The resistance $R_{12,34}$ can be calculated by linear fitting the $V_{1,2} \approx I_{3,4}$ curve (Figure S1c, Supporting Information). Likewise, $R_{23,14}$ can also be obtained by switching the points. The resistivity of the pellet can be calculated using the following equation:

$$e^{-\pi \cdot R_{12,43} \cdot d/\rho} + e^{-\pi \cdot R_{23,14} \cdot d/\rho} = 1 \quad (2)$$

where d (cm) refers to the thickness of the pellet. The electrical resistance ρ (Ω cm) is the inverse of the electrical conductivity σ (S cm^{-1}). MATLAB software was used to solve this implicit equation to obtain the value for ρ. The code is:

```
syms Res
d = 1; %% thickness, unit: mm (change the number if needed)
pi = 3.1415926; %% PI, unitless
R_1 = 10; %% resistance, unit: ohm (change the number if needed)
R_2 = 20; %% resistance, unit: ohm (change the number if needed)
Res_1 = solve(exp(-pi*R_1*d/Res)+exp(-pi*R_2*d/Res)-1, Res) %% note: In MATLAB, the "log" actually refers to "ln"
Res_2 = vpa(Res_1,10) %% calculate the final data to a value contain 10 significant digits
```

Electrochemical Measurements: To make different MnO_2-coated cathodes, 240 mg MnO_2 was mixed with 80 mg poly(vinylidene fluoride) (PVDF) and 80 mg Ketjenblack EC600JD carbon black in a quartz mortar and ground for 15 min. After being transferred into a 20 mL glass vial and added with 4 mL dimethylacetamide, the as-obtained slurry was kept stirred overnight and cast onto a graphite foil with doctor blade, followed by vacuum drying overnight at 70 °C. The coating amount of MnO_2 was quantified by inductively coupled plasma mass spectrometry after dissolving in an HCl solution.

Unless specified otherwise, in the Mn–H_2 batteries, flat graphite foil was used as the cathode-free current collector (0.5 cm^2), and 1 mg cm^{-2} Pt/C (40% Pt) on carbon paper (also named as gas diffusion electrode, GDE) (Fuel Cell Earth Co. EP401) was used as anode electrode with hydrogen flow rate of 5 mL min^{-1}. The electrolyte contained 100 mL of 1 mol L^{-1} $MnSO_4$ and 0.1 mol L^{-1} H_2SO_4 was used to ensure a sufficient supply of protons and Mn^{2+} for MnO_2 deposition and discharge. The cathode-to-anode distance is 1.5 mm without a separator. In the Mn–Zn batteries, graphite foil (0.5 cm^2) was used as the cathode-free current collector, and zinc plate was used as the anode. In the experiment with pre-coated MnO_2 cathode, 150 µL of 1 mol L^{-1} $ZnSO_4$ and 0.1 mol L^{-1} H_2SO_4 was used as the electrolyte; while in the experiments of the primary phase study, 700 µL 1 M $MnSO_4$ + 1 M $ZnSO_4$ was applied.

Higher temperatures indeed changed the deposited MnO_2 phase but could also increase the ion mobility in the electrolyte. To confirm that the better battery performance is mainly due to phase manipulation rather than ion-mobility, the battery was charged at high temperature to form the more conductive phases, then discharged at room temperature to exclude the effect of ionic mobility in the Mn–H_2 battery. One hundred fifty microliter of 1 M $MnSO_4$ + 0.1 M H_2SO_4 was used as the electrolyte to ensure fast cooling.

Long cycle performance evaluation was carried out by using 0.5 cm^2 carbon felt (6.13 mm thickness, 99.0%, Alfa Aesar) as the cathode-free current collector and Pt gas diffusion electrode as the anode electrode. Titanium foil (0.032 mm thick, 99.7%, Alfa Aesar) was used to connect both the cathode and anode electrodes to the potentiostat workstation (Figure 5a); glassy fiber was used as the separator. Battery was charged at 1.6 V to 20 mAh cm^{-2}, then discharged at 200 mA cm^{-2} followed by a deep discharge at 20 mA cm^{-2}, and then held at 0 V until the current was lower than 0.5 mA cm^{-2}. The cut-off voltage for discharge is 0 V. The discharged capacity includes both the discharged capacity at −200 and −20 mA cm^{-2} since the discharge plateau of −20 mA cm^{-2} could still be maintained at ≈1.2 V vs SHE (Figure S10, Supporting Information).

Please note that all the chemicals used were purchased from Sigma–Aldrich unless specified. A regular coin cell was not appropriate for the Mn^{2+}/MnO_2-based battery because the acid electrolyte could dissolve the coin cell. All experiments related to temperature control require 30 min

holding at the desired temperature before testing. All the electrochemical experiments were recorded by the VMP3 potentiostat (BioLogic). The battery was running at 25 °C unless specified.

Materials Characterizations: SEM images are obtained with a Thermo Fisher Scientific Apreo S LoVac scanning electron microscope under an accelerating voltage of 5 kV. To minimize the background signal from the substrates, a thin Kapton tape (25.4 µm thickness) was used to adhere to the as-deposited MnO_2 layer for the X-ray diffractometer (XRD) measurement. Mo radiation was selected as the high bright light source for XRD (Bruker D8) with an exposure duration of 300 s and a resolution of 0.1°.

Impedance Measurement on the Mn–H_2 Battery by Different Capacity Loading: The purpose of measuring the impedance of a Mn–H_2 battery is to confirm the higher electronic conductivity of the deposited MnO_2 phases at higher temperatures. Acrylic sheet and rubber were purchased from McMaster–Carr and laser-cut to fabricate the cell shown in Figure S11a (Supporting Information) (electrode area: 0.5 cm^2), where 1 mg cm^{-2} Pt/C (40% Pt) on carbon paper (also named as gas diffusion electrode, GDE) (Fuel cell earth Co. EP401) was used as the counter/ref electrode, and graphite foil (0.13 mm thickness, Alfa Aesar) was used as the working electrode. The distance between the counter and the working electrode was 1.5 mm. The electrolyte contained 150 µL 1 M $MnSO_4$ + 0.1 M H_2SO_4, and no separator was applied.

The electrochemical impedance spectroscopy was recorded using a VMP3 potentiostat (BioLogic). After the cell was charged to a certain capacity under 1.6 V and rested for 5 min to eliminate the concentration polarization, the impedance was monitored with 10 mV of AC signal in the frequency range from 1 MHz to 200 mHz. A typical impedance curve was shown in Figure S11b (Supporting Information), where the ohmic resistance (R_0) was taken out for comparison. The ohmic resistance R_0 could be divided into three parts:

$$R_0 = R_{\text{electrolyte}} + R_{\text{wire,current-collectors}} + R_{MnO_2} \quad (3)$$

where $R_{\text{wire,current-collectors}}$ are constant during the charging process. During the charging process, Mn^{2+} was consumed, a MnO_2 layer was formed, and proton was generated. Since the maximum charged capacity of MnO_2 (1 mAh cm^{-2}) only possessed <5% of the total Mn in the electrolyte and the thickness of 1 mAh cm^{-2} MnO_2 is ≈10 µm (Figure S12f, Supporting Information), which is far less than the distance between the cathode and anode (1.5 mm), the ohmic resistance could be hardly affected by Mn^{2+} and SO_4^{2-} concentration variation and distance change between the cathode and anode electrode during charging. However, the resistance decrease caused by the proton concentration increasing during charging is significant. By changing the electrolyte with different proton concentrations in Figure S11a (Supporting Information), the effect of proton concentration was corrected, such that the increment of R_0 (corrected) (Figure 3c) was mainly attributed to the non-conductivity of the deposited MnO_2 layer, meaning that the larger slope in Figure 3c indicated a larger electronic resistance of the deposited MnO_2 layer.

Supporting Information

Supporting Information is available from the Wiley Online Library or from the author.

Acknowledgements

X.X. and Z.Z. contributed equally to this work. The authors acknowledge the use and support of the Stanford Nano Shared Facilities and the Stanford Nanofabrication Facility. The authors extend their appreciation to Deputyship for Research & Innovation, Ministry of Education in Saudi Arabia for funding this research work. Z.Z. acknowledges the support of Stanford Interdisciplinary Graduate Fellowship. S.T.O. acknowledges the support of Knight Hennessy scholarship for graduate studies at Stanford University.

Conflict of Interest

The authors declare no conflict of interest.

Author Contributions

X.X., Z.Z., and Y.C. conceived the initial idea. X.X. and Z.Z. designed experiments. X.X. conducted electrochemical measurements. Y.W. performed the electronic conductivity measurement. R.X. and W.H. helped with the device fabrication. X.X., Z.Z., and Y.C. wrote the manuscript with input from all co-authors. X.X. acknowledges Dr. Chungheon Shin for the help on MnO_2 synthesis.

Data Availability Statement

The data that support the findings of this study are available from the corresponding author upon reasonable request.

Keywords

aqueous battery, electronic conductivity, gamma-MnO_2, grid-scale energy storage, MnO_2 polymorph

Received: December 10, 2022
Revised: April 5, 2023
Published online: July 6, 2023

[1] B. Dunn, H. Kamath, J.-M. Tarascon, *Science* **2011**, *334*, 928.
[2] D. Chao, W. Zhou, F. Xie, C. Ye, H. Li, M. Jaroniec, S.-Z. Qiao, *Sci. Adv.* **2020**, *6*, eaba4098.
[3] H. Zhang, X. Liu, H. Li, I. Hasa, S. Passerini, *Angew. Chem., Int. Ed.* **2021**, *60*, 598.
[4] J. Shin, D. S. Choi, H. J. Lee, Y. Jung, J. W. Choi, *Adv. Energy Mater.* **2019**, *9*, 1900083.
[5] F. Duffner, N. Kronemeyer, J. Tübke, J. Leker, M. Winter, R. Schmuch, *Nat. Energy* **2021**, *6*, 123.
[6] T. Xiong, Y. Zhang, W. S. V. Lee, J. Xue, *Adv. Energy Mater.* **2020**, *10*, 2001769.
[7] V. Mathew, B. Sambandam, S. Kim, S. Kim, S. Park, S. Lee, M. H. Alfaruqi, V. Soundharrajan, S. Islam, D. Y. Putro, J.-Y. Hwang, Y.-K. Sun, J. Kim, *ACS Energy Lett.* **2020**, *5*, 2376.
[8] M. Wang, X. Zheng, X. Zhang, D. Chao, S. Z. Qiao, H. N. Alshareef, Y. Cui, W. Chen, *Adv. Energy Mater.* **2021**, *11*, 2002904.
[9] H. Pan, Y. Shao, P. Yan, Y. Cheng, K. S. Han, Z. Nie, C. Wang, J. Yang, X. Li, P. Bhattacharya, K. T. Mueller, J. Liu, *Nat. Energy* **2016**, *1*, 16039.
[10] C. Xu, B. Li, H. Du, F. Kang, *Angew. Chem., Int. Ed.* **2012**, *51*, 933.
[11] W. Chen, G. Li, A. Pei, Y. Li, L. Liao, H. Wang, J. Wan, Z. Liang, G. Chen, H. Zhang, J. Wang, Y. Cui, *Nat. Energy* **2018**, *3*, 428.
[12] D. Chao, W. Zhou, C. Ye, Q. Zhang, Y. Chen, L. Gu, K. Davey, S. Qiao, *Angew. Chem., Int. Ed.* **2019**, *58*, 7823.
[13] G. Li, W. Chen, H. Zhang, Y. Gong, F. Shi, J. Wang, R. Zhang, G. Chen, Y. Jin, T. Wu, Z. Tang, Y. Cui, *Adv. Energy Mater.* **2020**, *10*, 1902085.
[14] C. Liu, X. Chi, Q. Han, Y. Liu, *Adv. Energy Mater.* **2020**, *10*, 1903589.
[15] C. Zhong, B. Liu, J. Ding, X. Liu, Y. Zhong, Y. Li, C. Sun, X. Han, Y. Deng, N. Zhao, W. Hu, *Nat. Energy* **2020**, *5*, 440.
[16] L. Cao, D. Li, T. Pollard, T. Deng, B. Zhang, C. Yang, L. Chen, J. Vatamanu, E. Hu, M. J. Hourwitz, L. Ma, M. Ding, Q. Li, S. Hou, K. Gaskell, J. T. Fourkas, X.-Q. Yang, K. Xu, O. Borodin, C. Wang, *Nat. Nanotechnol.* **2021**, *16*, 902.
[17] J. Zheng, Q. Zhao, T. Tang, J. Yin, C. D. Quilty, G. D. Renderos, X. Liu, Y. Deng, L. Wang, D. C. Bock, C. Jaye, D. Zhang, E. S. Takeuchi, K. J. Takeuchi, A. C. Marschilok, L. A. Archer, *Science* **2019**, *366*, 645.

[18] A. Singh, O. Sel, H. Perrot, V. Balland, B. Limoges, C. Laberty-Robert, *J. Mater. Chem. A* **2021**, *9*, 1500.
[19] J. Lei, Y. Yao, Z. Wang, Y.-C. Lu, *Energy Environ. Sci.* **2021**, *14*, 4418.
[20] K. W. Nam, H. Kim, J. H. Choi, J. W. Choi, *Energy Environ. Sci.* **2019**, *12*, 1999.
[21] L. Wei, L. Zeng, M. C. Wu, H. R. Jiang, T. S. Zhao, *J. Power Sources* **2019**, *423*, 203.
[22] S. He, J. Wang, X. Zhang, J. Chen, Z. Wang, T. Yang, Z. Liu, Y. Liang, B. Wang, S. Liu, L. Zhang, J. Huang, J. Huang, L. A. O'Dell, H. Yu, *Adv. Funct. Mater.* **2019**, *29*, 1905228.
[23] J. Huang, L. Yan, D. Bin, X. Dong, Y. Wang, Y. Xia, *J. Mater. Chem. A* **2020**, *8*, 5959.
[24] G. Liang, F. Mo, H. Li, Z. Tang, Z. Liu, D. Wang, Q. Yang, L. Ma, C. Zhi, *Adv. Energy Mater.* **2019**, *9*, 1901838.
[25] E. Hayashi, Y. Yamaguchi, K. Kamata, N. Tsunoda, Y. Kumagai, F. Oba, M. Hara, *J. Am. Chem. Soc.* **2019**, *141*, 890.
[26] F. Cheng, T. Zhang, Y. Zhang, J. Du, X. Han, J. Chen, *Angew. Chem., Int. Ed.* **2013**, *52*, 2474.
[27] Z. Y. Leong, H. Y. Yang, *ACS Appl. Mater. Interfaces* **2019**, *11*, 13176.
[28] S. Devaraj, N. Munichandraiah, *J. Phys. Chem. C* **2008**, *112*, 4406.
[29] K. Zhang, X. Han, Z. Hu, X. Zhang, Z. Tao, J. Chen, *Chem. Soc. Rev.* **2015**, *44*, 699.
[30] J.-G. Wang, Y. Yang, Z.-H. Huang, F. Kang, *Carbon* **2013**, *61*, 190.
[31] C. Xu, F. Kang, B. Li, H. Du, *J. Mater. Res.* **2010**, *25*, 1421.
[32] W. Wei, X. Cui, W. Chen, D. G. Ivey, *Chem. Soc. Rev.* **2011**, *40*, 1697.
[33] S. L. Suib, *Acc. Chem. Res.* **2008**, *41*, 479.
[34] D. Gentili, M. Gazzano, M. Melucci, D. Jones, M. Cavallini, *Chem. Soc. Rev.* **2019**, *48*, 2502.
[35] S. Ching, J. A. Landrigan, M. L. Jorgensen, *Chem. Mater.* **1995**, *7*, 1604.
[36] X. Wang, Y. Li, *Chem. Commun.* **2002**, 764.
[37] S. Liang, F. Teng, G. Bulgan, R. Zong, Y. Zhu, *J. Phys. Chem. C* **2008**, *112*, 5307.
[38] D. Li, G. Du, J. Wang, Z. Guo, Z. Chen, H. Liu, *J. Chin. Chem. Soc.* **2012**, *59*, 1211.
[39] D. M. Robinson, Y. B. Go, M. Greenblatt, G. C. Dismukes, *J. Am. Chem. Soc.* **2010**, *132*, 11467.
[40] O. Ghodbane, J.-L. Pascal, F. Favier, *ACS Appl. Mater. Interfaces* **2009**, *1*, 1130.
[41] R. N. De Guzman, A. Awaluddin, Y.-F. Shen, Z. R. Tian, S. L. Suib, S. Ching, C.-L. O'Young, *Chem. Mater.* **1995**, *7*, 1286.
[42] P. Strobel, J. Vicat, D. T. Qui, *J. Solid State Chem.* **1984**, *55*, 67.
[43] J.-C. Charenton, P. Strobel, *Solid State Ion.* **1987**, *24*, 333.
[44] T. R. Juran, J. Young, M. Smeu, *J. Phys. Chem. C* **2018**, *122*, 8788.
[45] N. Zhang, F. Cheng, J. Liu, L. Wang, X. Long, X. Liu, F. Li, J. Chen, *Nat. Commun.* **2017**, *8*, 405.
[46] W.-H. Lai, Y.-X. Wang, Y. Wang, M. Wu, J.-Z. Wang, H.-K. Liu, S.-L. Chou, J. Chen, S.-X. Dou, *Nat. Chem.* **2019**, *11*, 695.
[47] A. J. Cruz-Cabeza, S. M. Reutzel-Edens, J. Bernstein, *Chem. Soc. Rev.* **2015**, *44*, 8619.
[48] Y. Yuan, K. He, B. W. Byles, C. Liu, K. Amine, J. Lu, E. Pomerantseva, R. Shahbazian-Yassar, *Chem* **2019**, *5*, 1793.
[49] Y. Yuan, W. Yao, B. W. Byles, E. Pomerantseva, K. Amine, R. Shahbazian-Yassar, J. Lu, *Small Struct.* **2021**, *2*, 2000091.
[50] Y. Yuan, B. Byles, W. Yao, K. He, M. Cheng, J. Lu, K. Amine, E. Pomerantseva, R. Shahbazian-Yassar, *Microsc. Microanal.* **2018**, *24*, 1500.
[51] A. Biswal, B. C. Tripathy, K. Sanjay, T. Subbaiah, M. Minakshi, *RSC Adv.* **2015**, *5*, 58255.
[52] M. M. Sundaram, A. Biswal, D. Mitchell, R. Jones, C. Fernandez, *Phys. Chem. Chem. Phys.* **2016**, *18*, 4711.
[53] J. P. Rethinaraj, S. Visvanathan, *J. Power Sources* **1993**, *42*, 335.
[54] L. J. van der Pauw, *Philips Res. Rep.* **1958**, *13*, 1.